Local Strain Heterogeneity Influences the Optoelectronic Properties of Halide Perovskites

Timothy W. Jones[#1], Anna Osherov[#2], Mejd Alsari[#3], Melany Sponseller[2], Benjamin C. Duck[1], Young-Kwang Jung[4], Charles Settens[2], Farnaz Niroui[2], Roberto Brenes[2], Camelia V. Stan[6], Yao Li[6,7], Mojtaba Abdi-Jalebi[3], Nobumichi Tamura[6], J. Emyr Macdonald[8], Manfred Burghammer[9], Vladimir Bulović[2], Aron Walsh[4,5], Gregory J. Wilson[1], Samuele Lilliu[10,11], and Samuel D. Stranks*[2,3]

[1]CSIRO Energy Centre, Mayfield West NSW 2304, Australia

[2]Research Laboratory of Electronics, Massachusetts Institute of Technology, 77 Massachusetts Avenue, Cambridge, Massachusetts 02139, USA

[3]Cavendish Laboratory, University of Cambridge, JJ Thompson Avenue, Cambridge CB3 0HE, UK

[4]Department of Materials Science and Engineering, Yonsei University, Seoul 03722, Korea

[5]Department of Materials, Imperial College London, Exhibition Road, London SW7 2AZ, UK

[6]Advanced Light Source, Lawrence Berkeley National Laboratory, Berkeley, California 94720, USA

[7]Xi'an Jiaotong University, State Key Laboratory for Mechanical Behavior of Materials, Xi'an, China

[8]School of Physics and Astronomy, Cardiff University, Cardiff CF24 3AA, UK

[9]European Synchrotron Radiation Facility, Grenoble, France

[10]Department of Physics and Astronomy, University of Sheffield, Sheffield S3 7RH, UK

[11]The UAE Centre for Crystallography, UAE

[#]These authors contributed equally

*sds65@cam.ac.uk

Halide perovskites are promising semiconductors for optoelectronics, yet thin films show substantial microscale heterogeneity. Understanding the origins of these variations is essential for mitigating parasitic losses such as non-radiative decay. Here, we probe the structural and chemical origins of the heterogeneity by utilizing scanning X-ray diffraction beamlines at two different synchrotrons combined with high-resolution transmission electron microscopy to spatially characterize the crystallographic properties of individual micrometer-sized perovskite grains in high-quality films. We reveal new levels of heterogeneity on the ten-micrometer scale (super-grains) and even ten-nanometer scale (sub-grain domains). By directly correlating these properties with their corresponding local time-resolved photoluminescence properties, we find that regions showing the greatest luminescence losses correspond to strained regions, which arise from enhanced defect concentrations. Our work reveals remarkably complex heterogeneity across multiple length scales, shedding new light on the defect tolerance of perovskites.

Halide perovskite semiconductors have captured the imagination of the research community because of the unprecedented progress in performance of photovoltaic (PV) and light-emission devices, coupled with remarkably simple techniques for deposition and fabrication (*1*). In just six years, PV power conversion efficiencies (PCEs) have been lifted beyond 22%, along with reports of promising performances of perovskite light-emitting diodes (LEDs) (*2, 3*). However, an essential condition for PV and LED devices to reach their efficiency limits is a high radiative efficiency in which non-radiative losses are eliminated (*4*). Non-radiative recombination, for example recombination of electrons and holes mediated by defect traps in the bulk or at device interfaces, is a parasitic loss pathway that limits the open-circuit voltage in solar cells. The photoluminescence (PL) quantum efficiency (PLQE) of neat perovskite films under solar illumination conditions is low (typically <10%) (*5*); passivation post-treatments can substantially increase these values but are yet to entirely remove non-radiative losses especially in the presence of device electrodes (*6-8*). The important metric of external radiative efficiency for high-performance perovskite PV devices still remains ~1% (*9, 10*), far behind the 30% achieved by state-of-the-art GaAs cells (*11*).

Macroscopic observations of non-radiative losses in perovskite films are manifested as an emission heterogeneity on the microscale, where the PL lifetime and intensity have been shown to vary between different grains even in the highest-performing polycrystalline films (*12*). This microscale spatial heterogeneity has also been observed in charge carrier diffusion lengths (*13*) and in the photocurrent and open-circuit voltage in full solar cell devices (*14*). Together, these measurements demonstrate the impact of the microscale on the resulting macroscopic polycrystalline film properties, suggesting that there is enormous scope for improving device PCE by understanding and then addressing these heterogeneous optoelectronic properties. The literature consensus attributes non-radiative losses to a spatially-heterogeneous population of sub-bandgap electronic states that act as trap-mediated recombination sites (*12, 15*). The origin of these traps remains unconfirmed but they likely relate to halide vacancies (*7, 16*).

Structural defects have a strong influence on the charge-carrier lifetime and recombination in semiconductors and, typically, charged point defects make efficient non-radiative recombination centers (*17*). Most semiconductors are intolerant to the presence of defects, with typical defect densities in crystalline silicon devices required to be no larger than ~10^{8}–10^{10} cm^{-3} (*18*). In contrast, trap densities in polycrystalline perovskite films in high-performing devices have been determined to be relatively large (~10^{13}–10^{18} cm^{-3}) (*15, 19, 20*). This in fact suggests a remarkable defect tolerance in perovskite films that needs to be understood in the context of the nature of the trap states and any residual non-radiative losses. Grain boundaries are a likely locus for defects sites, and large grain sizes, as viewed from scanning electron microscope (SEM) images, are implicitly preferred. Furthermore, polycrystalline perovskite films have been reported to show some degree of strain, which directly influences the macroscopic optoelectronic properties and stability (*21-23*), though it is unclear how the strain varies on the microscale and affects local recombination. Here, we directly probe the heterogeneity of high-quality perovskite thin films on multiple length scales to reveal local strain-related structural defects and their direct impact on optoelectronic behavior.

High-quality polycrystalline methylammonium lead iodide ($MAPbI_3$) films were solution-processed on glass cover slips from lead-acetate and MAI-based precursor solutions containing hypophosphorous acid additives (*24*) (see Supplementary Material (SM) for methods). An SEM image of the film is shown in the inset of Fig. 1A, revealing grain sizes of ~0.5-1 μm, along with

an example of the uniquely-shaped Au particles solution-processed on the film surface to allow registering and correlating the same scan area between different experiments in this work. The films have a strong preferential orientation with the <110> and <220> planes as the primary observed reflections (see Fig. S1 for the full macroscopic X-ray diffraction (XRD) pattern). To structurally characterize the perovskite grains on the microscale we utilized the scanning micro-XRD (μXRD) beamline 12.3.2 at the Advanced Light Source (ALS) with a spatial resolution of ~2.5 μm (*25*). We held the samples under flowing nitrogen at 240 K during the measurements to minimize beam damage. The summed 2D powder pattern for a 70 × 70 μm^2 region indexes correctly to the tetragonal phase of $MAPbI_3$ and the chi-integrated diffractogram from the entire region matches the macroscopic diffractogram from a laboratory instrument apart from a temperature-related shift (Fig. 1A). The <220> and <222> are the dominant reflections in the μXRD patterns due to limitations in the experimental setup, which did not allow us to observe reflections below scattering vector q = 1.33 $Å^{-1}$ (Fig. S2). Line profiles show excellent match to tetragonal $MAPbI_3$ (*26*) and negligible traces of crystalline impurity peaks (see Fig. S3).

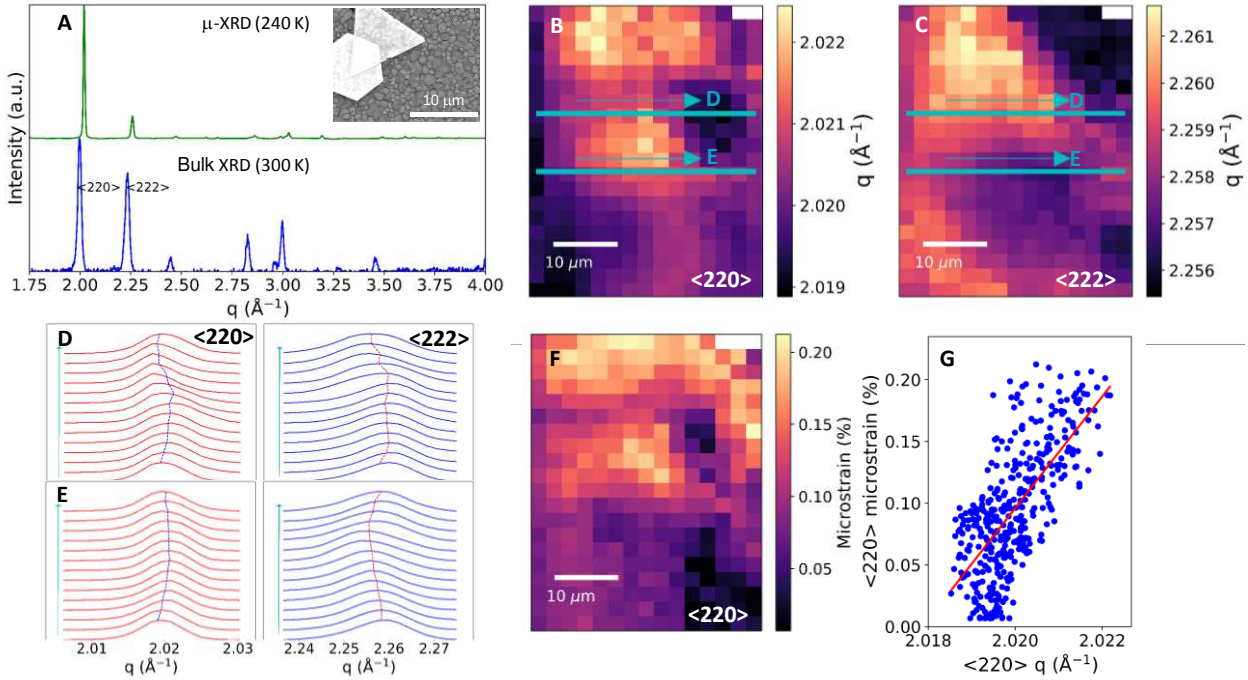

Figure 1. Characterizing structural heterogeneity in high-performance $MAPbI_3$ films by μXRD. (A) Comparison of the macroscopic bulk XRD pattern (300 K) with the micro-XRD pattern (240 K) summed over a 70 × 70 μm^2 spatial region, with the key reflections labelled. Inset: SEM image of the perovskite grains along with ten-micrometer-sized Au fiducial marker particles. (B) Local <220> and (C) <222> diffraction peak q maps reveal grain orientation heterogeneity. (D) and (E) Selected slices of the <220> (red) and <222> (blue) through the maps in (B) and (C) illustrating the complex strain patterns present within the film. Vertical lines indicate peak position as determined through peak profile fitting and are a guide to the eye. (F) Microstrain map for the <220> diffraction peak. (G) Scatter plot of the calculated microstrain and corresponding scattering vector q for the <220> diffraction peak. The solid line is a linear regression fit to the data, revealing a statistically-significant correlation (negligible p-value, see SM).

In Figure 1B and C we show the spatial maps of the peak scattering vector q of the azimuthally-integrated <222> and <220> peaks (see Fig. S4 for maps of peak intensities). These maps reveal distinct local structural heterogeneity on the scale of beam resolution, which is consistent with heterogeneous local surface grain orientations, preferred orientations or changes in level of crystallinity across the film. These distinct local patterns are evidence for regions that share similar crystallographic properties over a ten-micrometer scale (super-grains), a much larger scale than the grains observed in SEM images.

Fig. 1D and E show the μXRD patterns taken from horizontal slices as indicated by the colored lines on Fig. 1B and C. Subtle shifts in the peak position and broadening reveal the presence of detailed microscale structural heterogeneity. This heterogeneity in the local q vector for the <220> orientation of ~0.15%, corresponding to a spontaneous stress of ~19 MPa (based on a Young's Modulus of 12.8 GPa (*27*)), is typical of different regions of the films measured, and is a level of heterogeneity unobservable with laboratory diffraction techniques in both spatial resolution and peak variation (*28*). Interestingly, the μXRD slice in Figure 1D depicts a region with long-range parallel coupling between the two reflections in local q variation, whereas Figure 1E depicts a region with anti-parallel coupling between the two reflections (Fig. S5). We interpret these observations as evidence of complex local strain variations (*21*), and thus our results reveal long-range (>10 μm) strain patterns present throughout the polycrystalline film. Interestingly, we also find that passivating the sample through exposure to humid air and light soaking, which decreases the trap density and increases the luminescence (*8*), removes this curious coupling (Fig. S6), hinting at a relationship between local structure, defect distributions and luminescence.

After subtracting the instrumental contribution towards peak broadening of the azimuthally-integrated line profiles, we consider the extreme cases of contributions to peak broadening from microstrain-only and crystallite-size only, as defined by the Williamson-Hall formalism. The variance of the crystallite-size-only is considerably larger and thus we conclude that microstrain is the dominant contributor towards peak breadth in these samples (see SM and Fig. S7 for further discussion). We show the resulting microstrain map of the dominant <220> reflection in Fig. 1G (see Fig. S8 for <222>). This reveals that the microstrain also has a complex local heterogeneity with a typical magnitude of ~0.1-0.2 %, indicating that each grain cluster has its own local strain environment. Importantly, there is a strong correlation between q and microstrain for the <220> peak (Fig. 1F and Fig. S8 for the <222>). That is, XRD peaks with the larger local q (lower d-spacing) contain the largest structural broadening due to microstrain (and vice versa). This suggests that the strain in the polycrystalline films is compressive, i.e. acting to reduce the volume of the unit cell. We observe similar correlations in an alloyed 'triple cation' $MA_{0.15}FA_{0.79}Cs_{0.06}Pb(I_{0.85}Br_{0.15})_3$ sample, suggesting this observation can be generalised to other compositions (*29*) (Fig. S9).

In order to further investigate this long range behavior and its relationship to local grains, we performed scanning nanofocus XRD (nXRD) measurements at the ID13 beamline at the European Synchrotron Radiation Facility (ESRF) (Fig. S10) (*26*). A $MAPbI_3$ perovskite film prepared as discussed above was spin-coated onto a Si/SiO_2 substrate and the sample raster scanned with the nXRD setup (beam spot size 200 × 200 nm^2; see Methods for details). We show a quiver plot for the <110> orientation in Fig. 2A, where the value of χ_p for each diffraction spot is represented using an arrow with its centre located in the spatial position from which the diffraction spot was acquired, and with an orientation and colour corresponding to χ_p (*26*). Diffraction spots adjacent both in spatial coordinates and in reciprocal space coordinates were considered as

belonging to the same cluster, here indicated as 'super-grain' (see SEM for details). We highlight in bold two super-grains with the largest covered areas calculated as the number of pixels within the super-grain times the pixel area (400 × 400 nm^2). These also exhibit local strain (q) variations within their dimensions (Fig. 2B and C), consistent with the variations observed in μXRD results.

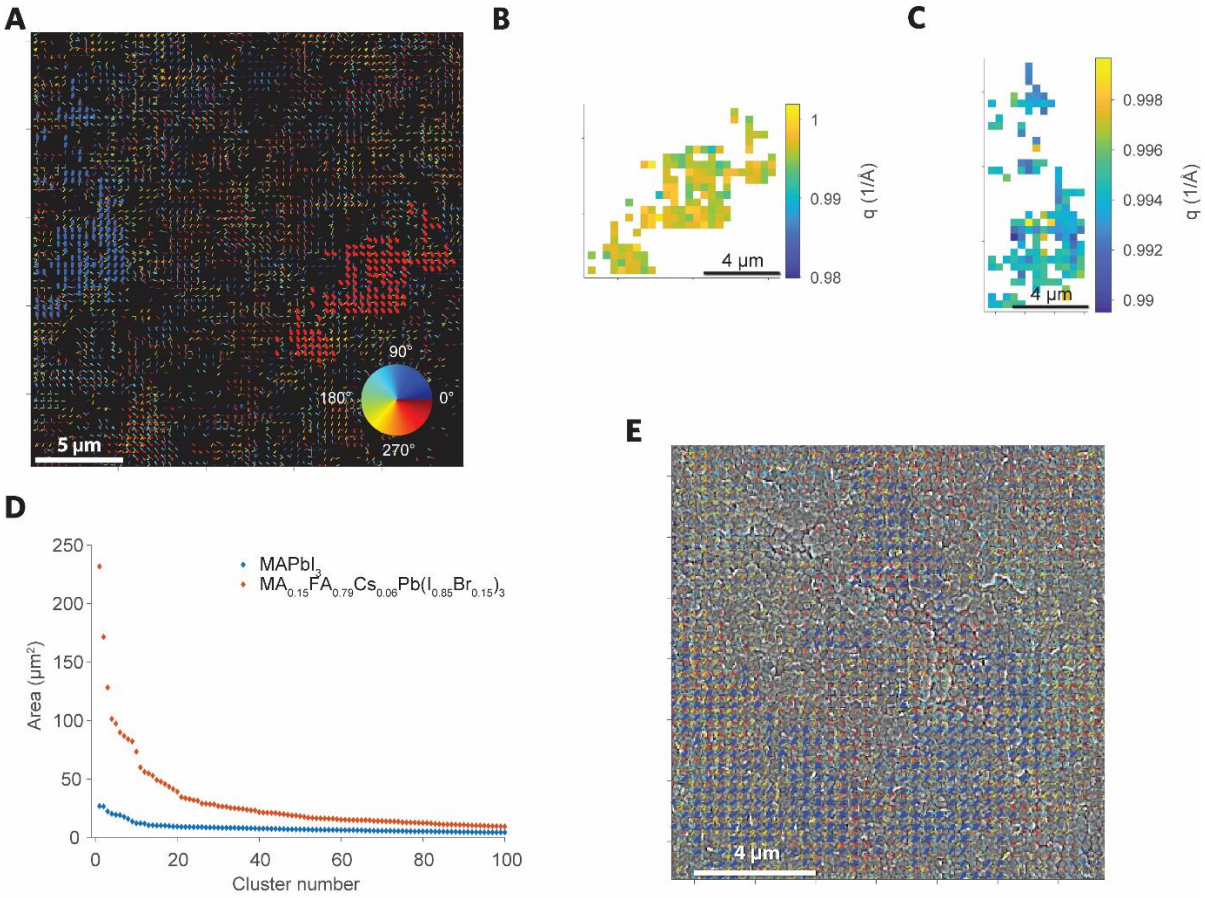

Figure 2. Nano-XRD measurements and super-grain analysis. (A) Quiver plot highlighting the first two largest super-grains showing the <110> reflection in a $MAPbI_3$ sample. (B,C) Absolute value of the scattering vector q extracted from the two largest super-grains in (A). (D) Super-grain size distributions for $MAPbI_3$ and $MA_{0.15}FA_{0.79}Cs_{0.06}Pb(I_{0.85}Br_{0.15})_3$. (E) Overlay between the quiver plot (<210>) and SEM scan in the same scan area for a $MA_{0.15}FA_{0.79}Cs_{0.06}Pb(I_{0.85}Br_{0.15})_3$ sample.

In Fig. 2D, we plot the super-grain sizes for the <110> reflection, showing that these largest regions cover an area of ~25 μm^2, extending well beyond the grain size observed in SEM images (~1 μm^2). We find this disparity is even more exaggerated in the triple cation $MA_{0.15}FA_{0.79}Cs_{0.06}Pb(I_{0.85}Br_{0.15})_3$ samples, which show super-grains as large as ~250 μm^2 (Fig. 2D) despite SEM grain sizes of only ~0.1 μm^2 ; this is clearly seen in the overlay of an SEM image and a quiver plot for the <210> reflection in Fig. 2E. This remarkable finding likely sheds light onto the apparent paradox whereby 'small-grain' triple cation perovskite films still attain the highest device PCE (*10*). Our results suggest that the critical grain size is actually the longer-range

structural super-grains rather than the grains viewed in SEM images. The formation of these large clusters with analogous orientation and facet control may have beneficial properties for carrier transport. The results also suggest that the grain orientation is non-random, with either templated nucleation/growth or fragmentation of larger grains for instance upon drying or annealing. Such a mechanism could be akin to the long-range co-orientation of crystal plates in echinoderms (*30*). These results highlight important new questions on nucleation and lateral carrier transport for the community.

To now explore crystallinity at a sub-grain resolution we turn to transmission electron microscopy (TEM). In Fig. 3A we show a cross-sectional bright-field TEM image of the Si<100>|perovskite interface. The sample was prepared by thinning down the 0.4 μm long lamella that appeared as an individual grain in the top-view SEM image by focused-ion beam (FIB). A selected-area electron diffraction (SAED) pattern obtained from a 200-nm region within the lamella is outlined by a circle in the micrograph and shown in the inset of Fig. 3A. The SAED pattern indicates a non-single crystalline nature of the "single grain" observed in SEM. Although the *d*-spacing corresponds to the tetragonal $MAPbI_3$ perovskite structure, the presence of elongated diffraction spots as well as a weak diffraction ring is a strong indicator of imperfections within the lattice that likely originate from strain and/or other defects.

To probe crystallinity at a deeper scale, a High-Resolution TEM (HR-TEM) micrograph was collected from a 70×70 nm^2 region (Fig. 3B). The HR-TEM micrograph shows a lack of lattice continuality in the tested area as indicated by the presence of domains and structural defects. Fast Fourier Transform (FFT) patterns generated from various 10×10 nm^2 regions of the HR-TEM micrograph are outlined by the colored boxes in Figure 3C and clearly demonstrate structural heterogeneity within a single grain. The regions marked by black and purple boxes possess near-identical diffraction patterns and are highly crystalline as indicated by the sharp diffraction spots. The identical *d*-spacing of the diffraction spots indicate a similarity in crystallinity and sub-grain crystallite orientation on the 10×10 nm^2 scale. The highly crystalline regions marked by the black and purple boxes contrasts with regions bound by the red and blue boxes. The markedly different patterns indicate the whole grain is not uniformly crystallized. The blue region is well-crystallized but shows the presence of more than one diffraction pattern. This might be a result of multi-grain overlap as well as indicate the presence of various structural defects such as a micro-twins or/and dislocations (*31*). In contrast, the red pattern shows a much weaker pattern indicting a poorly-crystallised or amorphous region within the same grain. While amorphization due to beam damage cannot be ruled out completely, a lack of homogeneity in the amorphization signature through the sample makes irradiation-induced amorphization less plausible.

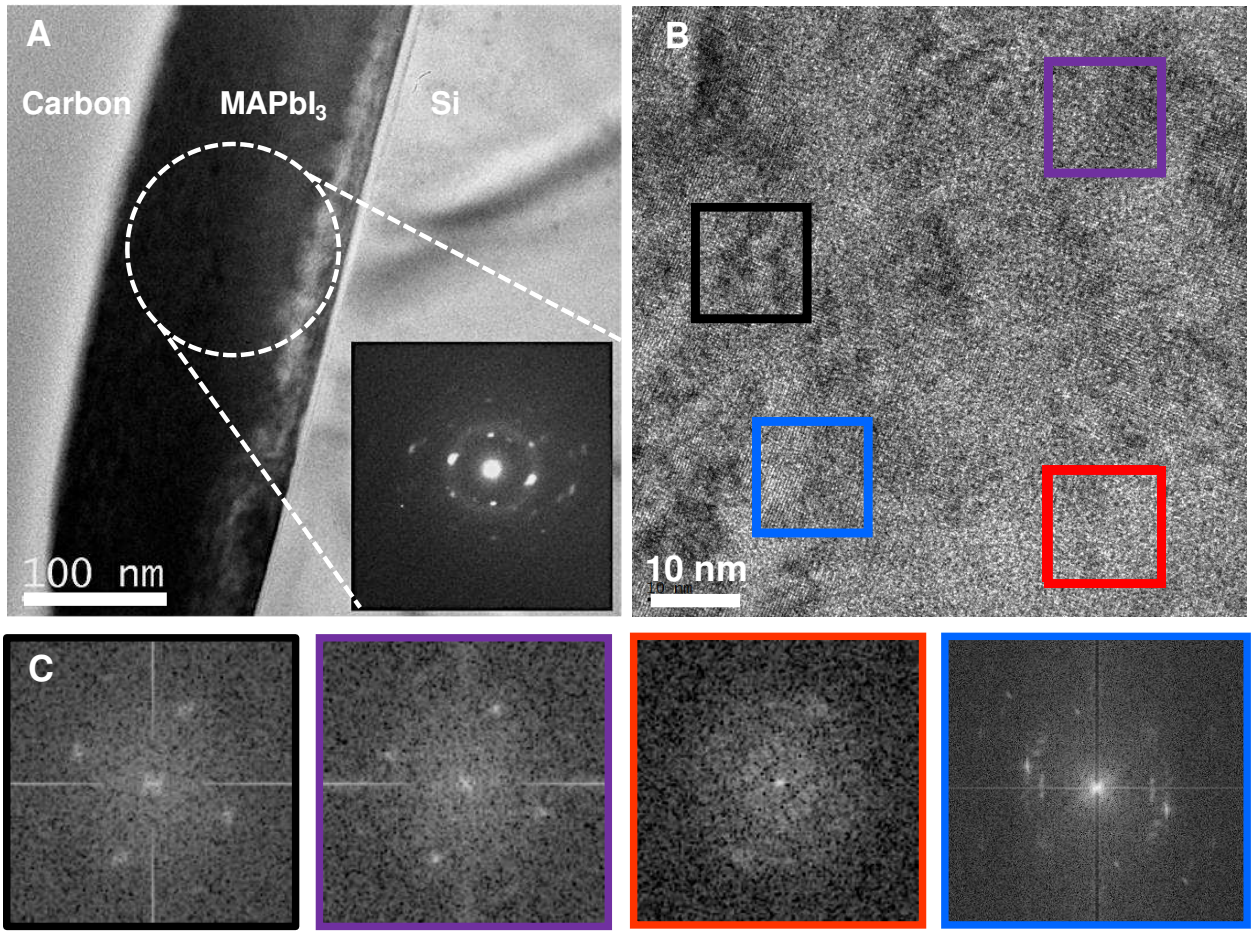

Figure 3. TEM electron diffraction analysis of $MAPbI_3$ perovskite grains from high performance films. (A) Cross-section image of single perovskite grain on Si<100> substrate and selected area electron diffraction (SAED) pattern collected from the region indicated (inset). (B) Higher-magnification TEM and (C) Fast Fourier transform (FFT) patterns generated across different regions of the grain shown in (B).

These results suggest that we need to re-think the conception of a perovskite grain as a single crystalline entity, for example as viewed in a SEM. Each of these entities are in fact comprised of many sub-crystallites on a ~10-100 nm scale above that of the unit cell but below that of a single grain. This scale of heterogeneity is consistent with recent reports showing lower symmetry domains below 20 nm (*32*) and substantial spatial variation in the photo-response of polycrystalline perovskite devices even within each grain (*14, 33, 34*). Further increasing complexity of the microstructure, our combined diffraction analysis demonstrates the existence of local grain clusters (super-grains) with shared crystal orientation and heterogeneous strain on the scale of tens of micrometers. We propose that this level of structure is imparted on the film during the stage of nucleation, where differences in local substrate morphology or local concentration differences during solution deposition template the growth of certain crystal planes.

To directly assess the impact of the observed strain on the optoelectronic properties, we correlate confocal PL measurements with μXRD measurements on the same scan area. We show

in Figure 4A a confocal PL intensity map. We note that here we are at sufficiently low excitation fluence that the local PL distribution is dominated by trap states rather than diffusion of carriers out of the local region (*35*). One striking observation is the presence of regional "clustering" of bright and dim grains. That is, grains are more likely to share similar fractions of radiative and non-radiative recombination pathways with their nearest neighbours. Local clustering of defects in strained regions is consistent with the XRD results above, again suggesting local structuring (super-grains) on a scale above that of the individual grain. We show the local time-resolved PL measurements of a bright cluster and a dim cluster in Fig. 4B representing the recombination of charge carriers. The bright regions have a longer PL lifetime than the dark regions, which is consistent with increased fractions of trap-limited recombination in the latter. We extract trap densities representative of the regions by fitting the decays with a kinetic model developed previously (*15*), quantifying the reduction in trap density from the dark (7.5×10^{16} cm^{-3}) to the bright (1×10^{16} cm^{-3}) regions.

To directly compare the PL maps with μXRD maps, we use the Au fiducial markers and an image analysis algorithm for image registration (see SM and Fig S11-14 for details). We show in the inset of Figure 4B the <220> μXRD peaks corresponding to the region with bright emission (long PL lifetime) and the region with dark emission (short PL lifetime). We find that the region with inferior emission intensity and carrier lifetime dynamics corresponds to a region with compressive-strained <220> lattice planes (i.e. larger q and increased peak broadening), whereas the region showing brighter emission and longer carrier lifetime is comparatively unstrained (i.e. smaller q and peak widths close to the instrumental broadening). We see these trends appear consistently across the maps; scatter plots of the relevant quantities across the map after accounting for differences in resolution between the techniques reveal a statistically-significant decrease in PL lifetime with <220> q (Fig. 4C) and with broadening (microstrain, Fig. 4D) (see Fig. S15 for example PL decays).

Using first-principles simulations, we have calculated the change in local defect concentrations in a strained crystal. For the charged iodine vacancy (V_I^+), the fraction of defective lattice sites from each is enhanced by a factor of 2 with respect to the unstrained crystal with 0.2% compressive strain in either the <110> or <111> direction (Fig. 4E). This is a lower bound as there will be a contribution of additional vacancies from uniaxial strain on each orientation, and the net increase in trap density is therefore consistent with the magnitude of the increase in trap density in a grain dark in PL relative to a bright grain, as calculated from the trap model above. These microscale observations are consistent with recent macroscopic laboratory-based measurements suggesting that reduced bulk strain leads to enhanced PL and charge carrier properties (*22, 23*). Our results show for the first time that the observation of local PL heterogeneity is substantially influenced by locally-heterogeneous strain distributions.

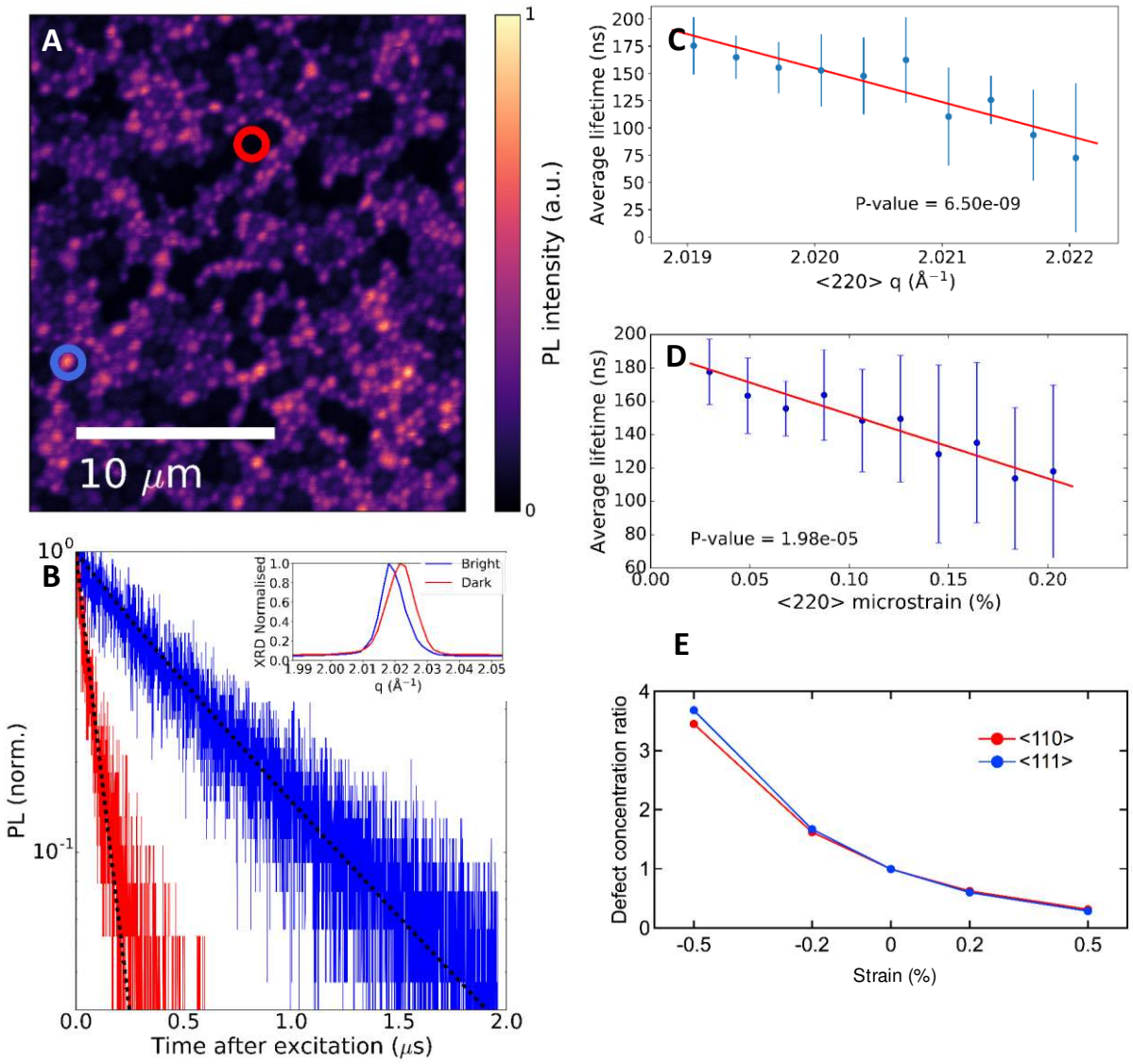

Figure 4. Correlating the microscale PL and local structural properties of high-performance $MAPbI_3$ films. (A) Confocal PL intensity map of a $MAPbI_3$ perovskite film with pulsed 405-nm excitation (0.5 MHz repetition rate, 0.1 μJ/cm^2/pulse). (B) Time-resolved PL decays of the bright (blue) and dark (red) regions highlighted in (A). The solid lines are fits to the data using a trap model to extract the electronic trap density, N_T (*15*). Inset: Highlighted <220> peak diffraction pattern for the bright and dark PL regions. Scatter plots of statistically-significant correlations between local PL lifetime and (C) local q (p-value = 5.9×10^{-9}) and (D) local broadening due to microstrain (p-value = 2.0×10^{-5}). (E) Ratio in concentration of V_I^+defects in <110> and <111> strained perovskite crystals to unstrained crystal, calculated from first-principles at T = 300 K.

Our work has revealed multiple length scales of structural heterogeneity, from long-range super-grain clusters, to grain-to-grain and sub-grain nanoscale variations. The exceptional performance of perovskites in spite of so many layers of disorder is truly remarkable, and is seemingly in contrast to established semiconductor physics. Indeed, the behaviour is similar to

liquid metals, which have highly disordered structures, yet maintain excellent charge transport properties (*36*). These observations also explain the high open-circuit voltages in devices even in the earliest stages of disordered crystallite formation (*37*). An interesting question arises about whether their exceptional performance is in fact *as a result of* the length scales and topology of the disorder. Future work will be required to consolidate our understanding of the complex relationships between physicochemical and optoelectronic properties, which would ultimately guide growth of films with optimal structural properties across all scales.

Acknowledgements : TWJ would like to acknowledge the Australian Renewable Energy Agency for receipt of a post-doctoral Fellowship. GJW would like to acknowledge the support of a CSIRO Julius Career Fellowship. TWJ and GJW are grateful to the International Synchrotron Access Program for travel support. This project has received funding from the European Union's Seventh Framework Programme (FP7/2007-2013) under REA grant agreement number PIOF-GA-2013-622630, the European Research Council (ERC) under the European Union's Horizon 2020 research and innovation programme (HYPERION, grant agreement No 756962), and the Royal Society and Tata Group (UF150033). This work made use of the Shared Experimental Facilities supported in part by the MRSEC Program of the National Science Foundation under award number MDR – 1419807. This work was supported in part by the Yonsei University Future-leading Research Initiative of 2017-22-0088. This research used resources of the Advanced Light Source, which is a DOE Office of Science User Facility under contract no. DE-AC02-05CH11231. We thank the European Synchrotron Radiation Facility (ESRF) for awarding beamtime at the ID13 beamline and the ID13 beamline staff for support with the measurements. M.A.J. thanks Nava Technology Limited and Nyak Technology Limited for their funding and technical support. AO would like to acknowledge the support from the NSF under Grant No. 1605406 (EP/L000202). M.A. received funding from 'The President of the UAE's Distinguished Student Scholarship Program (DSS), granted by the Ministry of Presidential Affairs'. The authors thank David Cahen and Gary Hodes for fruitful discussion.

References

1. S. D. Stranks, H. J. Snaith, Metal-halide perovskites for photovoltaic and light-emitting devices. *Nat. Nanotechnol.* **10**, 391-402 (2015).
2. W. S. Yang *et al.*, Iodide management in formamidinium-lead-halide-based perovskite layers for efficient solar cells. *Science* **356**, 1376-1379 (2017).
3. B. R. Sutherland, E. H. Sargent, Perovskite Photonic Sources. *Nat. Photon.* **10**, 295-302 (2016).
4. O. D. Miller, E. Yablonovitch, S. R. Kurtz, Strong Internal and External Luminescence as Solar Cells Approach the Shockley-Queisser Limit. *IEEE J. Photovolt.* **2**, 303-311 (2012).
5. S. D. Stranks, Nonradiative Losses in Metal Halide Perovskites. *ACS Energy Letters* **2**, 1515-1525 (2017).
6. D. W. deQuilettes *et al.*, Photoluminescence Lifetimes Exceeding 8 μs and Quantum Yields Exceeding 30% in Hybrid Perovskite Thin Films by Ligand Passivation. *ACS Energy Lett.* **1**, 438-444 (2016).
7. M. Abdi-Jalebi *et al.*, Maximising and Stabilising Luminescence in Halide Perovskite Device Structures Using Potassium-Halide Passivating Layers. *Nature* **In Press**, (2018).

8. R. Brenes *et al.*, Metal Halide Perovskite Polycrystalline Films Exhibiting Properties of Single Crystals. *Joule* **1**, 155-167 (2017).
9. C. Momblona *et al.*, Efficient vacuum deposited p-i-n and n-i-p perovskite solar cells employing doped charge transport layers. *Energy & Environmental Science* **9**, 3456-3463 (2016).
10. M. Saliba *et al.*, Incorporation of Rubidium Cations into Perovskite Solar Cells Improves Photovoltaic performance. *Science* **354**, 206-209 (2016).
11. M. A. Green, S. P. Bremner, Energy conversion approaches and materials for high-efficiency photovoltaics. *Nat. Mater.* **16**, 23-34 (2017).
12. D. W. deQuilettes *et al.*, Impact of microstructure on local carrier lifetime in perovskite solar cells. *Science* **348**, 683-686 (2015).
13. Z. Guo, J. S. Manser, Y. Wan, P. V. Kamat, L. Huang, Spatial and temporal imaging of long-range charge transport in perovskite thin films by ultrafast microscopy. *Nat. Commun.* **6**, 7471 (2015).
14. S. Y. Leblebici *et al.*, Facet-dependent photovoltaic efficiency variations in single grains of hybrid halide perovskite. *Nat. Energy* **1**, 16093 (2016).
15. S. D. Stranks *et al.*, Recombination Kinetics in Organic-Inorganic Perovskites: Excitons, Free Charge, and Subgap States. *Phys. Rev. Appl.* **2**, 034007 (2014).
16. R. Brenes, C. Eames, V. Bulovic, M. S. Islam, S. D. Stranks, The Impact of Atmosphere on the Local Luminescence Properties of Metal Halide Perovskite Grains. *Advanced Materials* **DOI: 10.1002/adma.201706208**, (2018).
17. A. M. Stoneham, Non-radiative transitions in semiconductors. *Reports on Progress in Physics* **44**, 1251 (1981).
18. J. R. Haynes, J. A. Hornbeck, Trapping of Minority Carriers in Silicon. II. n-Type Silicon. *Phys. Rev.* **100**, 606-615 (1955).
19. E. M. Hutter, G. E. Eperon, S. D. Stranks, T. J. Savenije, Charge Carriers in Planar and Meso-Structured Organic-Inorganic Perovskites: Mobilities, Lifetimes, and Concentrations of Trap States. *J. Phys. Chem. Lett.* **6**, 3082-3090 (2015).
20. Y. Yamada, M. Endo, A. Wakamiya, Y. Kanemitsu, Spontaneous Defect Annihilation in CH3NH3PbI3 Thin Films at Room Temperature Revealed by Time-Resolved Photoluminescence Spectroscopy. *J. Phys. Chem. Lett.* **6**, 482-486 (2015).
21. J. Zhao *et al.*, Strained hybrid perovskite thin films and their impact on the intrinsic stability of perovskite solar cells. *Science Advances* **3**, (2017).
22. D. P. McMeekin *et al.*, Crystallization Kinetics and Morphology Control of Formamidinium-Cesium Mixed-Cation Lead Mixed-Halide Perovskite via Tunability of the Colloidal Precursor Solution. *Adv Mater*, 1607039 (2017).
23. J. T.-W. Wang *et al.*, Efficient perovskite solar cells by metal ion doping. *Energy & Environmental Science* **9**, 2892-2901 (2016).
24. W. Zhang *et al.*, Enhanced optoelectronic quality of perovskite thin films with hypophosphorous acid for planar heterojunction solar cells. *Nat. Commun.* **6**, 10030 (2015).
25. M. Kunz *et al.*, A dedicated superbend x-ray microdiffraction beamline for materials, geo-, and environmental sciences at the advanced light source. *Review of Scientific Instruments* **80**, 035108 (2009).
26. S. Lilliu *et al.*, Mapping Morphological and Structural Properties of Lead Halide Perovskites by Scanning Nanofocus XRD. *Adv. Funct. Mater.* **26**, 8221-8230 (2016).

27. J. Feng, Mechanical properties of hybrid organic-inorganic CH3NH3BX3 (B = Sn, Pb; X = Br, I) perovskites for solar cell absorbers. *APL Materials* **2**, 081801 (2014).
28. S. Lilliu *et al.*, Mapping Morphological and Structural Properties of Lead Halide Perovskites by Scanning Nanofocus XRD. *eprint arXiv* **1606.04096**, (2016).
29. M. Saliba *et al.*, Cesium-Containing Triple Cation Perovskite Solar Cells: Improved Stability, Reproducibility and High Efficiency. *Energy Environ. Sci.* **9**, 1989-1997 (2016).
30. C. E. Killian *et al.*, Mechanism of Calcite Co-Orientation in the Sea Urchin Tooth. *Journal of the American Chemical Society* **131**, 18404-18409 (2009).
31. M. U. Rothmann *et al.*, Direct observation of intrinsic twin domains in tetragonal CH3NH3PbI3. *Nature Communications* **8**, 14547 (2017).
32. A. N. Beecher *et al.*, Direct Observation of Dynamic Symmetry Breaking above Room Temperature in Methylammonium Lead Iodide Perovskite. *ACS Energy Letters* **1**, 880-887 (2016).
33. Y. Kutes *et al.*, Mapping the Photoresponse of CH3NH3PbI3 Hybrid Perovskite Thin Films at the Nanoscale. *Nano Lett.* **16**, 3434-3441 (2016).
34. J. L. Garrett *et al.*, Real-time nanoscale open-circuit voltage dynamics of perovskite solar cells. *Nano Lett.* **17**, 2554–2560 (2017).
35. D. W. deQuilettes *et al.*, Tracking Photoexcited Carriers in Hybrid Perovskite Semiconductors: Trap-Dominated Spatial Heterogeneity and Diffusion. *ACS Nano* **11**, 11488-11496 (2017).
36. T. E. Faber, J. M. Ziman, A theory of the electrical properties of liquid metals. *Philosophical Magazine* **11**, 153-173 (1965).
37. M. Alsari *et al.*, In situ simultaneous photovoltaic and structural evolution of perovskite solar cells during film formation. *Energy & Environmental Science* **DOI: 10.1039/c7ee03013d**, (2018).